Research Article | Vol. 0, No. 0 / 00 00 0000 / Optical Materials Express 1

Optical Materials EXPRESS

Event detection via THz generation with flat nonlinear optics [Invited]

UNAI ARREGUI LEON,[1,*] PAOLO FRANCESCHINI,[2,3] OLGA SERGAEVA,[2] ANDREA TOGNAZZI,[3,4] DAVIDE ROCCO,[2,3] LUCA CARLETTI,[2,3] DOMENICO DE CEGLIA,[2,3] GIUSEPPE DELLA VALLE,[1,5,6] AND COSTANTINO DE ANGELIS[2,3]

[1] *Politecnico di Milano, Department of Physics, Piazza Leonardo da Vinci 32, Milano 20133, Italy*
[2] *University of Brescia, Department of Information Engineering, via Branze 38, 25123 Brescia, Italy*
[3] *National Institute of Optics, Consiglio Nazionale delle Ricerche, via Branze 45, 25123 Brescia, Italy*
[4] *University of Palermo, Dipartimento di Ingegneria, Viale delle Scienze, Palermo 90128, Italy*
[5] *Institute for photonics and nanotechnologies, Consiglio Nazionale delle Ricerche, Piazza Leonardo da Vinci 32, Milano 20133, Italy*
[6] *INFN Sezione di Milano, Istituto Nazionale di Fisica Nucleare, Via Celoria, 16, Milano 20133, Italy*
[*] *unai.arregui@polimi.it*

Abstract: Event detection is a key feature in many applications and is often achieved digitally by comparing sequential frames and detecting changes or patterns that signify an event. While digital systems dominate most applications, optical analog methods are receiving increasing attention in areas requiring speed or operation in challenging conditions. Here we demonstrate how a simple thin film of AlGaAs can be used to realize ultrafast event detection by exploiting the THz signal generated by the difference-frequency of optical events.

1. Introduction

Optical analog computing is widely acknowledged for its distinct advantages over other approaches, including low cross-talk and ultrafast processing speeds [1,2]. Initial efforts in this field aimed to replicate digital processing architectures by substituting electronic and optoelectronic switches with all-optical counterparts [3]. However, this approach was constrained by the need for large device volumes. Recently, a paradigm shift has occurred in all-optical analog image and signal processing, driven by advancements in flat-optics and photonic nanostructures [4]. The general concept has been already demonstrated in a variety of nanophotonic configurations, both in linear [5–11], and, more recently, also in nonlinear optical devices [12].

One particular and yet very relevant case of image and signal processing is edge detection in space (border recognition) and time (event recognition), crucial, for example, for computer vision [13–22]. It enables the identification of boundaries and structures within images, essential for tasks like object recognition, motion tracking, and scene understanding. In medical imaging, edge detection helps accurately delineate anatomical features, while in autonomous systems, it supports real-time navigation and obstacle avoidance. Additionally, in scientific research it facilitates the analysis of complex visual data, enhancing the detection of patterns and changes over time.

Edge detection is based on the suppression of unwanted low-frequency components (angular or temporal) because the information related to variation, such as event occurrence in time or the presence of a boundary in space, is encoded in the high-frequency components of the corresponding profile. Therefore, it is important to properly highlight the contribution from these high-frequency components via suitable methods. In linear devices, carefully designed metasurfaces provide the necessary shape of linear dispersion to retain only the high-frequency signals that correspond to edges [15,16]. In nonlinear devices, since the nonlinear output

#543944 https://doi.org/10.1364/OME.543944
Journal © 0000 Received 2 Oct 2024; revised 11 Dec 2024; accepted 11 Dec 2024; published 00 00 0000

Optical Materials EXPRESS

signal occurs in a different spectral region compared to the input ones, we gain an additional degree of freedom regarding the possibility to spectrally select the region where the largest variation of the event profile takes place. So edge detection entails avoiding the generation of undesired frequency components [12] as nonlinear interactions selectively generate the desired high-frequency components of the event profile, thus effectively highlighting the edges. This approach can be accomplished even in a thin film, without the need for a metasurface, although a carefully designed metasurface can provide an effective $\hat{\chi}^{(2)}(f)$ with "zero-crossing" in materials that do not naturally exhibit this feature. In the case of a spatial boundary, the spatial edge detection approach discussed in [12] provides the edges of an image in second-harmonic generation (SHG) using a circularly polarized pump (each linear component revealing the orthogonal edge) and a $\hat{\chi}^{(2)}(f)$ tensor of symmetry suitable for SHG that effectively computes the spatial derivative of the image. In the time domain, even a linearly polarized pump and a specific $\hat{\chi}^{(2)}(f)$ with a "zero-crossing" can provide temporal edges. This approach detects changes in time by eliminating nonlinear interactions at the "zero-crossing" frequency, thus revealing temporal variations.

Here, we propose a theoretical concept for temporal edge detection in a flat nonlinear layer with a second order nonlinearity $\chi^{(2)}$ (see Fig. 1). The events to be detected are contained in one or two time-dependent optical images ($S_{in}^{(a)}(x, y, t)$, $S_{in}^{(b)}(x, y, t)$), impinging on the nonlinear layer where difference-frequency generation (DFG) takes place; the events are then detected by monitoring the terahertz (THz) signal at the output of the flat nonlinear layer ($S_{out}(x, y, t)$), see 2(a).

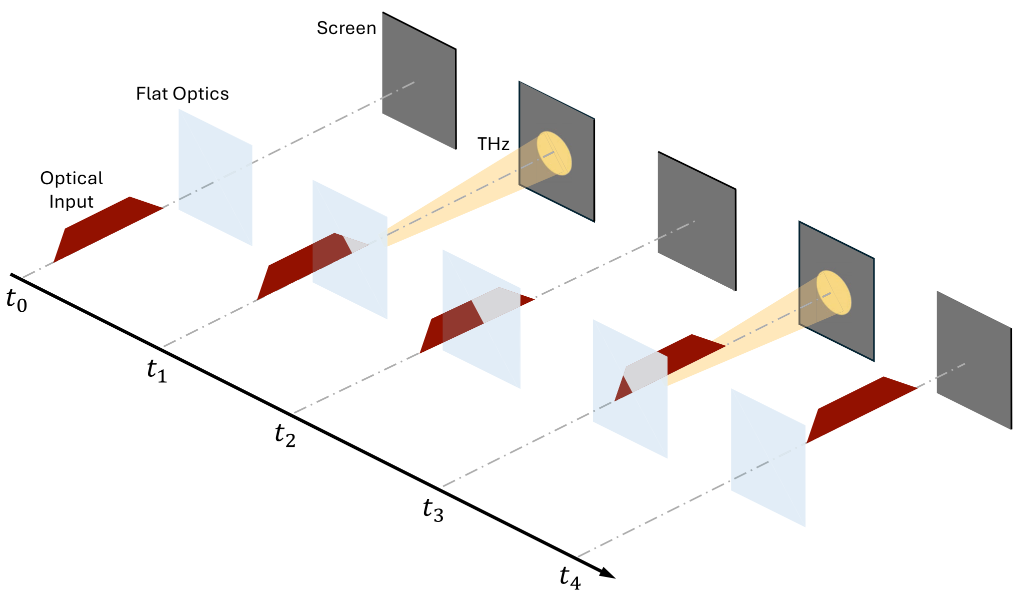

Fig. 1. Pictorial representation of THz event detection. At time instant t_0, an optical pulse, in red, is approaching a flat optical element endowed with nonlinear susceptibility. At time t_1, the rising edge of the input pulse impinges onto the flat optics and generate a THz signal via nonlinear generation processes. While the top part of the optical pulse envelope (with constant amplitude) is passing through the flat optics (t_2), no event detection is triggered because no variation of the optical signal is happening. At time t_3, a THz signal is generated due to the variation of the optical pulse profile related to the falling edge.

THz generation by difference-frequency of optical signals dates back to 1965 when it was first studied in crystalline quartz [23]; this finding was then followed by other research in different materials such as GaAs [24,25], GaP [26] or $LiNbO_3$ [27,28], including also the more newly

Optical Materials EXPRESS

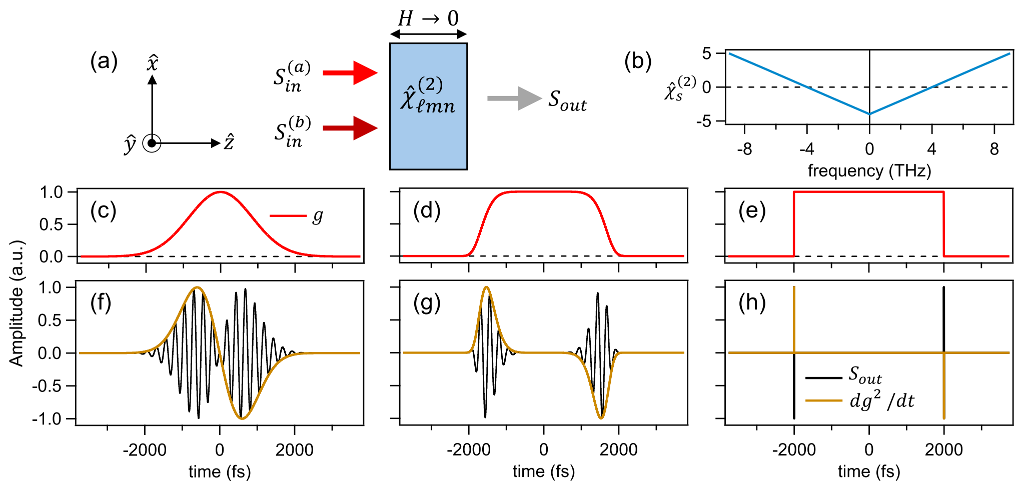

Fig. 2. Nonlinear Temporal Edge Detection Operating Principle. (a) Two input signals, $S_{in}^{(a)}(t)$ and $S_{in}^{(b)}(t)$, with carrier frequencies in the optical region, f_a and f_b, and temporal envelopes $g_a(t)$ and $g_b(t)$ impinge on a flat-optics element endowed by second-order response $\hat{\chi}_{\ell mn}^{(2)}$, defined in the spatial frame shown on the left-hand side of the panel. The output signal $S_{out}(t)$ is oscillating at $f_{THz} = |f_a - f_b|$. The derived model belongs to the limit of vanishing thickness, i.e. $H \rightarrow 0$. (b) Spectral properties of the considered ideal surface $\hat{\chi}_s^{(2)}$ susceptibility. (c-h) Illustrative examples of the nonlinear edge detection procedure in the case of pulse envelopes $g_a(t) = g_b(t) = g(t)$. (c-e) Input pulse envelope: Gaussian (c), Supergaussian (d), and Flat-Top (e). (f-h) Output function (black solid line) and its corresponding slow envelope term (yellow solid line) calculated with Eq. (5) from the panels c, d, and e, respectively. In these simulations we assumed $f_{THz} = 4$ THz.

employed organic crystals (DAST, HMQ-TMS...) [29]. The interest in broadening the bandwidth of THz sources unveiled the process of optical rectification (OR) of ultrashort laser pulses (i.e. intrapulse DFG) and works dealing with GaAs, CdTe, InP, and ZnTe emerged in [30–32].

Following the development of nanophotonics and biased by the ability of nanopatterned metallic structures to enhance optical fields in a sub-wavelength region, the research on generating terahertz radiation at the nanoscale predominantly focused on plasmonic platforms [33–35]. In this framework, the potential of metallic metamaterials for performing spatiotemporal differentiation via spoof surface plasmon-polaritons has also been theoretically and experimentally demonstrated in the microwave regime [36]. Recently, in view of circumventing the intrinsic optical loss present in metals, the idea of THz generation using all-dielectric nanoantennas and metasurfaces emerged [37–39], along with phonon-enhanced optical-to-THz conversion in them [40–42].

The coupling of THz fields with infrared-active lattice vibrations leads to a highly dispersive nonlinear response function of non-centrosymmetric polar semiconductors. In particular, the real part of $\hat{\chi}^{(2)}(f)$ follows a linear trend around "zero-crossing" points in the THz-frequency domain, bringing dielectric platforms into the spotlight of temporal signal processing. Indeed, flat optical elements allow to overcome the losses that accompany the $\hat{\chi}^{(2)}(f)$ "zero-crossing" by preventing absorption of THz radiation.

The key physical feature we propose here to demonstrate the event detection is the possibility of having an intrinsic or engineered extrinsic low efficiency THz generation at a particular frequency f_0 (*i.e.* $\hat{\chi}^{(2)}(f_0) \simeq 0$). THz frequencies around f_0 will be highly suppressed and consequently the electric field envelope at f_0 will contain only edges in time of the input signals, i.e. the events. In

Optical Materials EXPRESS

section 2, we present in detail the concept for an ideal situation; to introduce the key ideas we consider here a zero thickness nonlinear layer with an ideal second-order nonlinearity. In section 3, we consider AlGaAs as a representative example of a realistic material in the zero-thickness approximation; remarkably, we note that our device will naturally provide edge detection both in time and in space. Section 4 contains the full-wave numerical simulations of the device behavior both in time and in frequency domain; we consider here the realistic case of finite thickness and AlGaAs material parameters to show very good agreement with the simplified theoretical description presented in the previous sections. Finally, we also show how the nonlinear THz event detection signal can be enhanced by patterning the thin film of a $\chi^{(2)}$ medium at the nanoscale, i.e. by resorting to a metasurface $\chi^{(2)}$.

2. Concept demonstration

Here, we provide a detailed demonstration, in an ideal reference scenario, of how our flat-optics structure can perform analog temporal differentiation of the product of two time-dependent images, $S_{in}^{(a)}(x,y,t)$ and $S_{in}^{(b)}(x,y,t)$, conveyed by optical waves at frequencies f_a and f_b, respectively. The setup shown in Fig. 2 refers to this ideal reference situation for which the second-order nonlinear flat-optics element is uniform in the transverse plane and has zero thickness, and therefore is concentrated at $z = 0$. Moreover, in this ideal case, the second-order response $\hat{\chi}^{(2)}$ is assumed to be real with a pure linear dependence on frequency in the THz spectral region. Each element of the tensor describing the second-order nonlinear response of the sheet can then be written as (see Fig. 2(b)):

$$\hat{\chi}^{(2)}_{\ell mn}(x,y,z,f) \propto (|f| - f_0)\,\delta(z) = \hat{\chi}^{(2)}_s(f)\delta(z)\,, \tag{1}$$

where $f_0 = |f_a - f_b|$, we are assuming $\ell = y, m = x, n = x$ and we are omitting the subscripts in the final notation. The subindex s has been added to the $\hat{\chi}^{(2)}_s(f)$ susceptibility to stress that it is a *surface* nonlinearity (see the Supplement 1 for more details). In the next section, we will discuss how a good approximation of this ideal reference scenario can be achieved either using the natural intrinsic dispersion of the second-order nonlinear coefficients or by engineering a proper metasurface mimicking this behavior. In the rest of this section, after providing an overview of the nonlinear flat-optics analog temporal differentiation, we will focus on specific application examples leading to event occurrence recognition (*i.e.*, temporal edge detection) at the difference-frequency.

As sketched in Fig. 2(a), the flat-optics element, endowed by a second-order response, receives the signal inputs, $S_{in}^{(a)}(x,y,t)$ and $S_{in}^{(b)}(x,y,t)$, in the form of electric fields and provides as output the emitted electric field at THz frequency $S_{out}(x,y,t)$, which, in turn, is proportional to the nonlinear polarization density (see the Supplement 1 for more details).

Specifically, the time evolution of each input electric field can be expressed as

$$\begin{gathered} E_{in}^{(k)}(x,y,t) = \left(g_k(x,y,t)\cdot \mathrm{e}^{i2\pi f_k t} + c.c.\right) \\ k = a,b \end{gathered} \tag{2}$$

where $g_k(x,y,t)$ describes the pulse temporal envelope with time duration σ_p (full-width at half maximum, FWHM) and $c.c.$ denotes the complex conjugate.

The second-order surface polarization induced on the flat optics element is given by [43]

$$P_s^{(2)}(x,y,t) \propto \int_0^{\infty} d\tau_1 \int_0^{\infty} d\tau_2\, \chi_s^{(2)}(\tau_1,\tau_2) E_{in}(x,y,t-\tau_1) E_{in}(x,y,t-\tau_2), \tag{3}$$

where $E_{in}(x,y,t) = E_{in}^{(a)}(x,y,t) + E_{in}^{(b)}(x,y,t)$ is the total field in the polarized sheet and $\chi_s^{(2)}(\tau_1,\tau_2)$ takes into account a noninstantaneous nature, i.e. the frequency dispersion of the second-order

Optical Materials EXPRESS

response of the flat-optics element. The polarization in Eq. (3) can in principle contain a non-vanishing spectrum at frequencies corresponding to all possible second-order processes. However, as mentioned in the Supplement 1, we will filter such a spectrum to remain only with the signal generated around the THz carrier frequency $f_{THz} = f_0 = |f_a - f_b|$ by the difference-frequency generation process. Assuming that the bandwidth of the input electric field envelope is smaller than the THz carrier frequencies, *i.e.*, $\sigma_p^{-1} \ll f_{THz}$, Eq. (3) can be recast in the form (see the Supplement 1 for the derivation):

$$P_s^{(2)}(x,y,t) \propto \frac{-i}{\pi}\left[\frac{\partial}{\partial t}\Big(g_a(x,y,t)g_b^*(x,y,t)\Big)\cdot \mathrm{e}^{i2\pi f_{THz}t} - c.c.\right]. \tag{4}$$

Moreover, by assuming real pulse envelopes $g_a(x,y,t)$ and $g_b(x,y,t)$, the second-order sheet polarization can be written in the following compact expression

$$P_s^{(2)}(x,y,t) \propto \frac{1}{\pi}\sin(2\pi f_{THz}t)\frac{\partial}{\partial t}\Big(g_a(x,y,t)g_b(x,y,t)\Big), \tag{5}$$

showing that the output of the difference-frequency process occurring in the flat-optics element corresponds to the first derivative of the product of the input fields and it oscillates at frequency $f_{THz} = f_0$. Note that, consistently with the choice of ℓ, m, n we have done in Eq. (1), we have assumed the input fields to be both parallel to $\hat{x}$ and the induced polarization is parallel to $\hat{y}$, so that in the paraxial approximation we will not have extra space derivatives in the radiated field.

Here, the specific choice of the linear profile of $\chi^{(2)}$ in frequency domain allows to obtain only the contribution from the first-order time derivative of the input signals, thus providing the best condition for event detection. This is a key aspect when comparing the present approach to spatial edge detection; indeed, in the latter case, the only requirement is that $\chi^{(2)}$ possesses the proper symmetry to generate nonlinear signal, while here an additional requirements regarding the dispersion are introduced.

As illustrative examples, we consider three different shapes of the input pulse envelopes (see the Supplement 1 Sec. 3 for more details), *i.e.*, Gaussian, Supergaussian, and Flat-Top (see Fig. 2(c), (d), and (e), respectively), and we compute the corresponding output function (Fig. 2(f), (g), and (h), respectively) obtained in the case of real valued second-order susceptibility as in Fig. 2(b). For the sake of simplicity, here we neglect the spatial dependence, and we assume that in each of the three cases $g_a(x,y,t) = g_b(x,y,t) = g(t)$. To better show the results, panels 2(f), (g), and (h) display both the output function $S_{out}(t) \propto P^{(2)}(t)$ (black solid line) and its envelope (yellow solid line), where the latter highlights the time instants at which the maximum variation of $g^2(t)$ takes place. These results confirm the ability of the proposed flat-optics element to perform event detection.

3. Demonstration with a realistic material

In this section, we still refer to an ideal flat-optics element (uniform in the transverse plane and with zero thickness). However, we consider realistic material dispersion: $\hat{\chi}_s^{(2)}$ is not purely real and exhibits a nonlinear behavior as a function of frequency. We demonstrate that, also in this more realistic case, the behavior described in the previous section can still be achieved. As a realistic and widely used material, we chose AlGaAs, which has desirable bulk $\hat{\chi}^{(2)}(f)$ properties (Fig. 3), namely "zero-crossing" and quasi-linear frequency dependence of the real part around f_{THz} =5.635 THz ($Al_{0.18}Ga_{0.82}As$). The $\hat{\chi}^{(2)}$ frequency dependence of AlGaAs is approximated as in [42] neglecting the dispersion in the optical region, which in the cubic crystallographic

Optical Materials EXPRESS

frame reads:

$$\hat{\chi}^{(2)}_{\alpha\beta\gamma}(f_1, -f_2) = \delta^{eee}_{\alpha\beta\gamma}(\varepsilon_\infty - 1)^3 + \sum_{p=1}^{N} \delta^{i_p ee}_{\alpha\beta\gamma} \frac{S_p f_{0p}^2}{f_{0p}^2 - f_3^2 + i f_3 \gamma_p} (\varepsilon_\infty - 1)^2 \tag{6}$$

with $\alpha \neq \beta \neq \gamma$, f_3 being the frequency in the THz spectral range and f_1, f_2 the frequencies in the optical domain (for the rest of the parameters see the Supplement 1). We adopt the engineering phase convention $e^{+i\omega t}$ and Fourier transform pair in the form of Eqs. S3 and S9 in the Supplement 1. Note also that a thin film of $\langle 110 \rangle$-cut AlGaAs is consistent with the choice of $(\ell, m, n) = (y, x, x)$ cartesian laboratory frame indices in Eq. (1) [44]. The real and imaginary parts of AlGaAs $\hat{\chi}^{(2)}_{\alpha\beta\gamma}$ are shown in Fig. 3 in the THz and optical ranges and in Fig. 4(a) for the THz frequency range of interest, with "zero-crossing" location f_{THz} of the real part of $\hat{\chi}^{(2)}$ marked by thin grey horizontal and vertical lines.

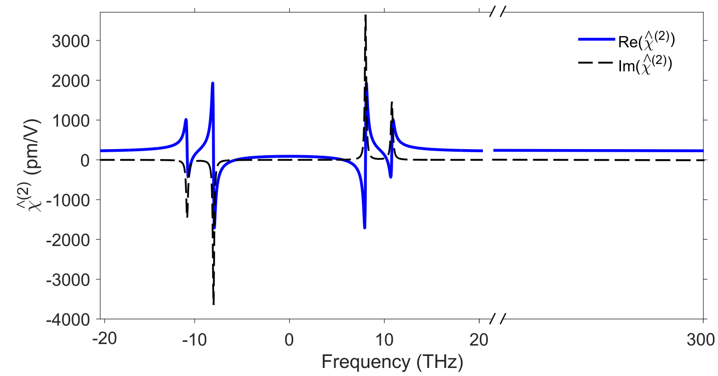

Fig. 3. Real (solid blue) and imaginary (dashed black) parts of $Al_{0.18}Ga_{0.82}As$ $\hat{\chi}^{(2)}$ calculated with Eq. (6).

As an example, we take as input signals two Gaussian pulses in near-infrared (NIR) range (wavelengths around 1030 nm and 1010 nm (Fig. 4(c), light green E_a and light blue E_b)); for the sake of brevity, we neglect the spatial dependence of the input beams and we focus our attention only on their temporal behavior, which reads

$$E^{(k)}_{in}(t) = A_k \exp\left(-\frac{(t - t_0)^n}{\sigma^n_{pk}}\right)\cos(2\pi f_k t), (k = a, b; n = 2) \tag{7}$$

with $\sigma_{pa} = 1$ ps and $\sigma_{pb} = 2\sigma_{pa}$ FWHM pulse durations, $t_0 = 0$, amplitudes $A_a = 1$ MV/m, and $A_b = 1.2$ MV/m, central frequencies $f_b = 291.06$ THz and $f_a = f_b + f_{THz} = 296.7$ THz. The amplitudes and pulse durations are chosen for illustrative purposes and can be different. Starting from here we use two pulses with very different temporal duration in contrast to Sec. 2. Our simulations demonstrate that the DFG signal detects the temporal edges of the product of the two input pulses that coincides with the shortest pulse edges for various pulse shape configurations. The duration of a shorter pump signal (signal of interest) is important because it defines the spectral width of the signal in the frequency domain. If the pulse is too short (for this case it should be longer than 300 fs), the DFG signal spectral range will be too wide, covering frequencies at which the $\hat{\chi}^{(2)}$ function demonstrates undesired nonlinear behavior with resonances concealing the weaker "zero-crossing" effect. If the pump pulse is too long, its spectral width is too narrow - not covering enough frequencies around the "zero-crossing" to generate a large enough DFG signal.

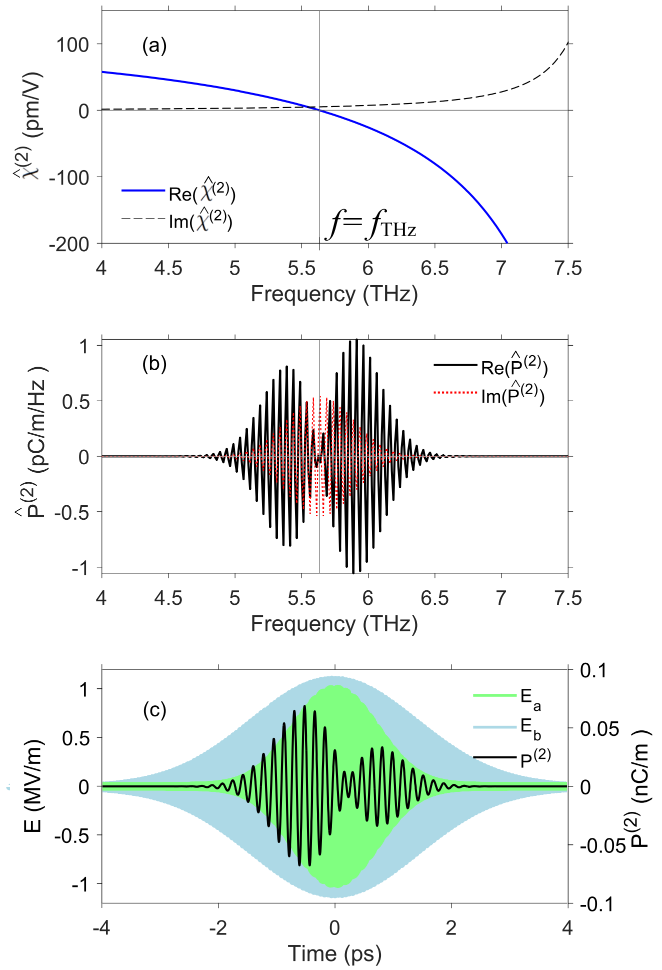

Fig. 4. Simulation results with $\hat{\chi}^{(2)}$ of AlGaAs. (a) Real (solid blue) and imaginary (dashed black) parts of AlGaAs $\hat{\chi}^{(2)}$ (Eq. (6)) with thin grey horizontal and vertical lines marking the "zero-crossing" location f_{THz}. (b) Frequency domain plots of nonlinear polarization $\hat{P}_s^{(2)}(f)$ (Eq. (S1)) real (solid black) and imaginary (dashed red) parts generated in AlGaAs with $\hat{\chi}^{(2)}$ from (a) by interaction of E_a and E_b (in (c)). The frequency range on the plot 4-7.5 THz corresponds to the filtered range. (c) Time domain plots of Gaussian pump pulses (light green E_a and blue E_b, (Eq. (7))) with durations $\sigma_{pa} = 1$ ps and $\sigma_{pb} = 2$ ps at 291 THz and (291 THz + f_{THz}) with induced DFG nonlinear polarization at around $f_{THz} \approx 5.635$ THz (solid black) calculated via inverse Fourier transform of $\hat{P}_s^{(2)}(f)$ in (b).

At this point, to model the device behavior, we use the above described material properties (assuming, in this ideal scenario, that the bulk $\hat{\chi}^{(2)}$ of AlGaAs is concentrated at $z = 0$). Using Matlab we transformed our pump signals (Eq. (7)) from the time domain into the frequency domain via Fourier transform of Eq. (S3); then we calculated the complex-valued nonlinear surface polarization $\hat{P}_s^{(2)}(f)$ (Eq. (S1), (Fig. 4(b)), and applied frequency filtering (4-7.5 THz) to filter out sum frequency generation and other possible nonlinear effects outside the frequency region of interest. Using the inverse Fourier transform we calculated $P^{(2)}(t)$ in time domain, which is depicted in Fig. 4(c) with the black curve. $P^{(2)}(t)$ is purely real and clearly reveals the temporal edges of the product of the two input pulses (similarly to Fig. 2(f)), here it coincides

Optical Materials EXPRESS

with the edges of the shorter pulse (signal of interest, E_a). The shape of the imaginary part $\Im(\hat{\chi}^{(2)}(f))$ in Fig. 4(a) results in the asymmetry of $P^{(2)}(t)$ (Fig. 4(c)) having larger values in the first part of the generated signal. For constant $\Im(\hat{P}^{(2)}(f))$ (or, more generally, for a $\Im(\hat{P}^{(2)}(f))$ with even symmetry around the working frequency) the nonlinear polarization $P^{(2)}(t)$ would be symmetric and its amplitudes for positive and negative times would be equal.

4. Full-wave simulation results

In this section, we remove the ideal zero thickness hypothesis and consider the physical situation where our flat optics device has a finite thickness. Here, we present full-wave simulations in COMSOL Multiphysics in both time and frequency domains. Both approaches demonstrate temporal edge detection and are in good agreement with the results from the theoretical surface model presented in the previous sections.

As well known, simulations in the frequency and time domains offer complementary advantages. The frequency domain is more efficient for modeling narrowband signals, longer pulses, and continuous-wave (CW) excitation. However, the time domain approach excels at simulating short pulses with broad frequency bandwidths, which would demand extensive resources in the frequency domain.

4.1. Time domain simulation

We performed time domain simulations in COMSOL Multiphysics of the temporal edge detection with the THz DFG process in a 400 nm ⟨100⟩-AlGaAs film on a sapphire substrate illuminated by linearly polarized pump supergaussian (n=8 in Eq. (7)) pulses with $\sigma_p = 2$ ps duration. These pulses are modeled as Gaussian beams under the paraxial approximation.

Considering $\hat{\chi}^{(2)}$ tensor in AlGaAs (Eq. (S25) in the Supplement 1) we chose the geometry of the excitation where both pulses propagate along the z-axis, and are polarized along x and y, respectively. The pulses are incident from the substrate side on a AlGaAs film at an angle $\alpha = 45°$, since the normal incidence configuration does not result in measurable DFG. The DFG signal generated within the AlGaAs film is influenced by reflection and transmission at the interfaces, governed by Snell's laws, resulting in a generally elliptically polarized signal. Each polarization component (x and y) exhibits similar behavior in detecting the temporal edges of the input pulses, so we plot only one component.

We included the frequency dispersion of refractive index and nonlinear susceptibility in the time domain simulation by using single (for $\hat{n}(f)$ and $\hat{k}(f)$) and multiple Lorentz oscillators approach (for $\hat{\chi}^{(2)}$) (solving in COMSOL Eqs. (S29) and (S31) from the Supplement 1).

We calculate excitation and nonlinear generation in the time domain, and to extract the data about the DFG we perform Fourier transform and frequency filtering (4 to 7.5 THz). The inverse Fourier transform converts the DFG signal back into the time domain to demonstrate the temporal edge detection (see Fig. 5) similarly to Fig. 2(g). The reduced amplitude at positive times and nonzero nonlinear signal in the middle arise from the nonlinear profile of $\Im(\hat{\chi}^{(2)}(f))$. Additionally, multiple internal reflections occurring at the sapphire/AlGaAs and AlGaAs/air interfaces contribute to the observed signal.

4.2. Frequency domain simulation

For the frequency domain simulation, we consider a scenario in which one of the optical pumps is a continuous-wave (CW) signal and the second one has a certain modulation bandwidth (information signal). This situation, with respect to the previous results where both signals had a finite bandwidth, is closer to a realistic application where the CW pump is used to control the THz range at which the DFG will take place. If the CW is chosen to be spectrally separated from the center of the information signal by f_0 (the "zero-crossing" frequency of Re $(\hat{\chi}^2)$), then the

Optical Materials EXPRESS

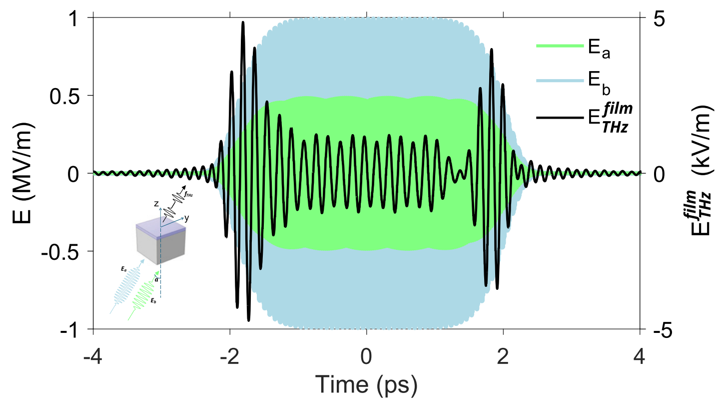

Fig. 5. Comsol time domain simulation. Time domain plots of the 2 ps supergaussian (power n = 8) with different amplitudes pump pulses at 291 THz (E_a, green) and at 296.7 THz (E_b, blue) with the transmitted DFG E_{THz}^{film} signal at $f_{THz} \approx 5.6$ THz (solid black) calculated in COMSOL for AlGaAs 400 nm film on a sapphire substrate. Excitation from the substrate, collection in the air (2 um from the surface of the film). An angle of incidence of $\alpha = 45°$ (see inset) is assumed.

nonlinearly emitted THz electric field will contain the time-derivative of the information signal alone.

In this simulation, we first calculated the spectra of our rectangular signal of interest E_a. We then performed a frequency-domain sweep of nonlinear generation, considering all combinations of frequency components of our input pulse with the CW carrier frequency. These were filtered in the range of 4–7.5 THz. Finally, we applied an inverse Fourier transform to obtain the time-domain result demonstrated in Fig. 6.

Figure 6(a) demonstrates that such functionality can be obtained from a 400 nm thick ⟨100⟩-AlGaAs thin film standing on a sapphire substrate. In the simulated scenario, a CW (at $\lambda_{CW} = 1030$ nm) and an optical carrier ($\simeq 5.6$ THz apart) modulated by a rectangular pulse, both linearly polarized, illuminate the thin film at oblique incidence (45° with respect to the surface normal). The output THz field (shown in black in Fig. 6(a)) clearly shows two strong peaks at the steps of the information signal (reminiscent of Fig. 2(h) with nonidealities explained above). Besides, note that the surface model (Fig. 6(a), purple) discussed in section 2 above and derived in the Supplement 1 is able to reproduce the frequency domain simulation results, allowing a much more straightforward estimation of the THz output from such flat-optics platforms.

In order to enhance the efficiency of such an event detection device, in Fig. 6(b) we show how a nanostructured AlGaAs metasurface can boost the THz field. The metasurface is constituted by a square array of nanopillars (radius $a = 160$ nm and height $h = 400$ nm) with a periodicity of 400 nm, also laying above a sapphire substrate. For such design parameters, the metasurface constituents hold a magnetic dipolar resonance at $\lambda_{CW} = 1030$ nm that allows to obtain a 2-fold enhancement with respect to the unpatterned slab. The generated DFG signal is elliptically polarized, but we show only one polarization component because the other component exhibits the same temporal behavior with a different amplitude, while both components similarly identify the temporal edges of the information signal. This is also consistent with future experimental realisation relying on electro-optical detection, allowing detection of the component that is parallel to the polarization of the optical probe signal.

Optical Materials EXPRESS

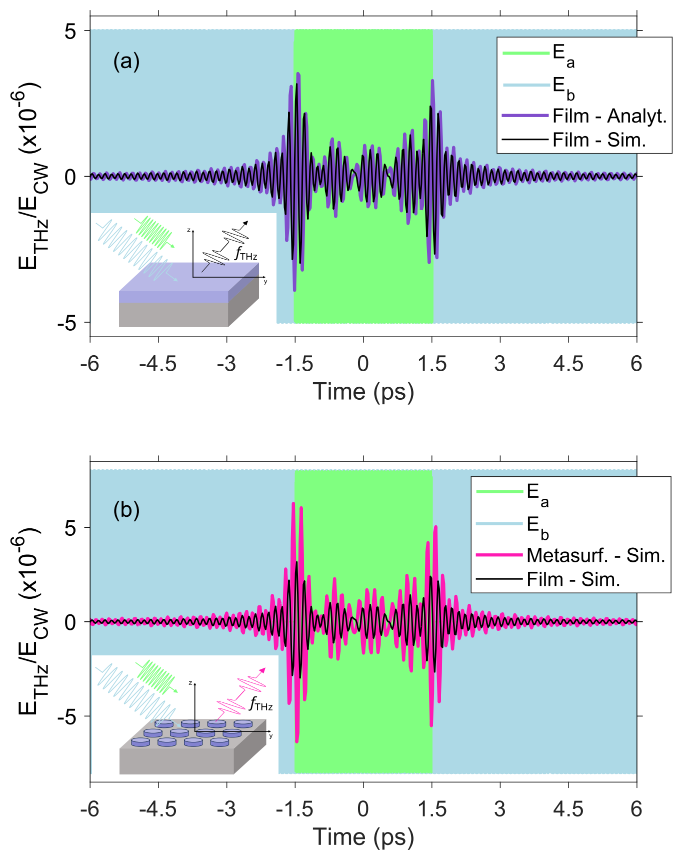

Fig. 6. Frequency domain Comsol simulation results for the edge detection of an optical rectangular pulse, with steps at $t = \pm 1.5$ ps. (a) The nonlinear THz field radiated by the AlGaAs thin film according to the surface analytical model (purple) developed in the Supplement 1 (Eqs. (S22)-(S24)), together with that coming from the COMSOL simulation of a 400 nm slab (black). (b) The simulated 400 nm slab result (black) is shown together with the (magenta) signal emitted by its nanopatterned version (metasurface). In both panels, the THz field is normalized to the amplitude of the CW pump (blue-colored background); the green background corresponds to the input rectangular pulse (information signal). E_a and E_b are linearly polarized and shown not to scale. In addition, the thin film and the metasurface both operate in reflection (illumination and detection in air domain, at 45° from the surface normal). The insets show the excitation geometry.

5. Conclusion

We showed that difference-frequency generation in the THz range in AlGaAs film allows for the detection of the pump pulse temporal edges, which promises possible applications in events or motion detection. Additionally, we show that metasurfaces are ideal platform candidates for such purposes, since they provide enhanced THz signal amplitude compared to thin films. The effect can be also demonstrated in other materials like $LiNbO_3$ or a metasurface that can be used to design the desired nonlinear response.

Funding. PRIN (P2022RFF9K, 2022BC5BW5, 2022H7RR4F, 2020EY2LJT); Horizon 2020 Framework Programme (899673); Italian National Recovery and Resilience Plan (NRRP) - NextGenerationEU (PE00000001, C79J24000190004). Q1

Acknowledgment. The authors acknowledge financial support by the European Union – Next Generation EU, Mission 4 Component 1 - PRIN PNRR 2022 project FLAIRS (P2022RFF9K), PRIN 2022 project GRACE6G (2022H7RR4F), PRIN 2022 project NO LIMITHz (2022BC5BW5), PRIN 2020 project METEOR (2020EY2LJT). This work was partially supported by the European Union under the Italian National Recovery and Resilience Plan (NRRP) of NextGenerationEU, of partnership on "Telecommunications of the Future" (PE00000001 - program "RESTART"), S2 SUPER – Programmable Networks, Cascade project PRISM - CUP: C79J24000190004. This publication is also part of the METAFAST project that received funding from the European Union Horizon 2020 Research and Innovation programme under Grant Agreement No. 899673. This work reflects only the authors views, and the European Commission is not responsible for any use that may be made of the information it contains.

Disclosures. The authors declare no conflicts of interest.

Data Availability. Data underlying the results presented in this paper are not publicly available at this time but may be obtained from the authors upon reasonable request.

Supplemental document. See Supplement 1 for supporting content.

References

1. D. R. Solli and B. Jalali, "Analog optical computing," Nat. Photonics **9**(11), 704–706 (2015).
2. P. L. McMahon, "The physics of optical computing," Nat. Rev. Phys. **5**(12), 717–734 (2023).
3. H. Gibbs, *Optical Bistability: Controlling Light with Light* (Academic Press, 1985).
4. A. Silva, F. Monticone, G. Castaldi, *et al.*, "Performing mathematical operations with metamaterials," Science **343**(6167), 160–163 (2014).
5. A. Pors, M. G. Nielsen, and S. I. Bozhevolnyi, "Analog computing using reflective plasmonic metasurfaces," Nano Lett. **15**(1), 791–797 (2015)
6. N. V. Golovastikov, D. A. Bykov, L. L. Doskolovich, *et al.*, "Spatial optical integrator based on phase-shifted Bragg gratings," Opt. Commun. **338**, 457–460 (2015).
7. A. Youssefi, F. Zangeneh-Nejad, S. Abdollahramezani, *et al.*, "Analog computing by Brewster effect," Opt. Lett. **41**(15), 3467–3470 (2016).
8. A. Chizari, S. Abdollahramezani, M. V. Jamali, *et al.*, "Analog optical computing based on a dielectric meta-reflect array," Opt. Lett. **41**(15), 3451–3454 (2016). Publisher: Optica Publishing Group.
9. A. Overvig and A. Alù, "Diffractive Nonlocal Metasurfaces," Laser Photonics Rev. **16**(8), 2100633 (2022).
10. M. Cotrufo, A. Arora, S. Singh, *et al.*, "Dispersion engineered metasurfaces for broadband, high-NA, high-efficiency, dual-polarization analog image processing," Nat. Commun. **14**(1), 7078 (2023).
11. J. Hu, D. Mengu, D. C. Tzarouchis, *et al.*, "Diffractive optical computing in free space," Nat. Commun. **15**(1), 1525 (2024).
12. D. de Ceglia, A. Alù, D. N. Neshev, *et al.*, "Analog image processing with nonlinear nonlocal flat optics," Opt. Mater. Express **14**(1), 92–100 (2024).
13. H. Kwon, D. Sounas, A. Cordaro, *et al.*, "Nonlocal metasurfaces for optical signal processing," Phys. Rev. Lett. **121**(17), 173004 (2018).
14. W. J. Padilla and R. D. Averitt, "Imaging with metamaterials," Nat. Rev. Phys. **4**(2), 85–100 (2021).
15. Y. Zhou, H. Zheng, I. I. Kravchenko, *et al.*, "Flat optics for image differentiation," Nat. Photonics **14**(5), 316–323 (2020).
16. S. Esfahani, M. Cotrufo, and A. Alù, "Tailoring space-time nonlocality for event-based image processing metasurfaces," Phys. Rev. Lett. **133**(6), 063801 (2024).
17. A. Saba, M. R. Tavakol, P. Karimi-Khoozani, *et al.*, "Two-dimensional edge detection by guided mode resonant metasurface," IEEE Photonics Technol. Lett. **30**(9), 853–856 (2018).
18. J. Zhou, H. Qian, C.-F. Chen, *et al.*, "Optical edge detection based on high-efficiency dielectric metasurface," Proc. Natl. Acad. Sci. **116**(23), 11137–11140 (2019).
19. O. Y. Long, C. Guo, H. Wang, *et al.*, "Isotropic topological second-order spatial differentiator operating in transmission mode," Opt. Lett. **46**(13), 3247–3250 (2021).
20. A. Komar, R. A. Aoni, L. Xu, *et al.*, "Edge detection with Mie-resonant dielectric metasurfaces," ACS Photonics **8**(3), 864–871 (2021).
21. A. Cordaro, B. Edwards, V. Nikkhah, *et al.*, "Solving integral equations in free space with inverse-designed ultrathin optical metagratings," Nature Nanotechnology **18**, 365-372 (2023).
22. M. Cotrufo, S. Esfahani, D. Korobkin, *et al.*, "Temporal signal processing with nonlocal optical metasurfaces," NPJ Nanophoton. **1**, 39 (2024).
23. F. Zernike and P. R. Berman, "Generation of far infrared as a difference frequency," Phys. Rev. Lett. **15**(26), 999–1001 (1965).
24. R. Aggarwal, B. Lax, and G. Favrot, "Noncollinear phase matching in GaAs," Appl. Phys. Lett. **22**(7), 329–330 (1973).
25. B. Lax, R. L. Aggarwal, and G. Favrot, "Far-infrared step-tunable coherent radiation source: 70 μm to 2 mm," Appl. Phys. Lett. **23**(12), 679–681 (1973).
26. T. Tanabe, K. Suto, J. Nishizawa, *et al.*, "Tunable terahertz wave generation in the 3- to 7-THz region from GaP," Appl. Phys. Lett. **83**(2), 237–239 (2003).

27. D. H. Auston, A. M. Glass, and P. LeFur, "Tunable far-infrared generation by difference frequency mixing of dye lasers in reduced (black) lithium niobate," Appl. Phys. Lett. **23**(1), 47–48 (1973).
28. K. H. Yang, J. R. Morris, P. L. Richards, *et al.*, "Phase-matched far-infrared generation by optical mixing of dye laser beams," Appl. Phys. Lett. **23**(12), 669–671 (1973).
29. S.-J. Kim, B. J. Kang, U. Puc, *et al.*, "Highly nonlinear optical organic crystals for efficient terahertz wave generation, detection, and applications," Adv. Opt. Mater. **9**(23), 2101019 (2021).
30. S. L. Chuang, S. Schmitt-Rink, B. I. Greene, *et al.*, "Optical rectification at semiconductor surfaces," Phys. Rev. Lett. **68**(1), 102–105 (1992).
31. A. Rice, Y. Jin, X. F. Ma, *et al.*, "Terahertz optical rectification from ⟨110⟩ zinc-blende crystals," Appl. Phys. Lett. **64**(11), 1324–1326 (1994).
32. J. Ahn, A. V. Efimov, R. Averitt, *et al.*, "Terahertz waveform synthesis via optical rectification of shaped ultrafast laser pulses," Opt. Express **11**(20), 2486–2496 (2003).
33. D. K. Polyushkin, E. Hendry, E. K. Stone, *et al.*, "THz generation from plasmonic nanoparticle arrays," Nano Lett. **11**(11), 4718–4724 (2011). PMID: 22007706.
34. C. W. Berry and M. Jarrahi, "Terahertz generation using plasmonic photoconductive gratings," New J. Phys. **14**(10), 105029 (2012).
35. L. Luo, I. Chatzakis, J. Wang, *et al.*, "Broadband terahertz generation from metamaterials," Nat. Commun. **5**(1), 3055 (2014).
36. Y. Zhou, J. Zhan, Z. Xu, *et al.*, "Electromagnetic spatiotemporal differentiation meta-devices," Laser Photonics Rev. **17**(11), 2300182 (2023).
37. L. Hu, B. Wang, Y. Guo, *et al.*, "Quasi-BIC enhanced broadband terahertz generation in all-dielectric metasurface," Adv. Opt. Mater. **10**(12), 2200193 (2022).
38. L. L. Hale, H. Jung, S. D. Gennaro, *et al.*, "Terahertz pulse generation from GaAs metasurfaces," ACS Photonics **9**(4), 1136–1142 (2022).
39. H. Jung, L. L. Hale, S. D. Gennaro, *et al.*, "Terahertz pulse generation with binary phase control in nonlinear InAs metasurface," Nano Lett. **22**(22), 9077–9083 (2022). PMID: 36367359.
40. U. Arregui Leon, D. Rocco, L. Carletti, *et al.*, "THz-photonics transceivers by all-dielectric phonon-polariton nonlinear nanoantennas," Sci. Rep. **12**(1), 1–11 (2022).
41. L. Carletti, C. McDonnell, U. Arregui Leon, *et al.*, "Nonlinear THz generation through optical rectification enhanced by phonon–polaritons in lithium niobate thin films," ACS Photonics **10**(9), 3419–3425 (2023).
42. U. Arregui Leon, L. Carletti, D. Rocco, *et al.*, "THz generation via optical rectification in nanomaterials: Universal modeling approach and effective $\bar{\chi}^{(2)}$ description," Laser Photonics Rev. **18**(2), 2300669 (2024).
43. R. W. Boyd, *Nonlinear Optics* (Academic Press, 2008), 3rd ed.
44. L. Xu, G. Saerens, M. Timofeeva, *et al.*, "Forward and backward switching of nonlinear unidirectional emission from GaAs nanoantennas," ACS Nano **14**(2), 1379–1389 (2020).